



Lanthanide doped nanoheaters with reliable and absolute temperature feedback



Gabriel López-Peña^a, Khouloud Hamraoui^b, Karima Horchani-Naifer^b, Christoph Gerke^{c,f}, Dirk H. Ortgies^{e,f}, Emma Martín Rodríguez^a, Guanying Chen^d, Daniel Jaque^{e,f,*}, Jorge Rubio Retama^{a,f}

^a Nanomaterials for Bioimaging Group (NanoBIG), Departamento de Física Aplicada, Facultad de Ciencias, Universidad Autónoma de Madrid, Madrid, 28049, Spain

^b Faculty of Mathematical, Physical and Natural Sciences of Tunis (FST) & Laboratory of Physical Chemistry of Mineral Materials and their Applications, National Center for Researches in Materials Sciences, Technopole of Borj Cedria, BP 73, 8027, Soliman, Tunisia

^c Departamento de Química en Ciencias Farmacéuticas, Facultad de Farmacia, Universidad Complutense de Madrid, Plaza Ramón y Cajal S/N, Madrid, 28040, Spain

^d MIT Key Laboratory of Critical Materials Technology for New Energy Conversion and Storage, School of Chemistry and Chemical Engineering & Key Laboratory of Micro-systems and Micro-structures, Ministry of Education, Harbin Institute of Technology, 150001, Harbin, PR China

^e Nanomaterials for Bioimaging Group (NanoBIG), Departamento de Física de Materiales, Facultad de Ciencias, Universidad Autónoma de Madrid, Madrid, 28049, Spain

^f Nanomaterials for Bioimaging Group (NanoBIG), Instituto Ramón y Cajal de Investigación Sanitaria IRYCIS, Ctra Colmenar Km 9-100, Madrid, 28034, Spain

ARTICLE INFO

Keywords:

Lanthanide-doped nanoparticles
Photothermal therapy
Luminescence nanothermometry
Temperature
Lifetime

ABSTRACT

The development of selective and controlled photo-thermal therapies requires luminescent nanoparticles capable of simultaneous heating and contactless thermal sensing. Until now, thermal therapies have suffered from a lack of control over the absolute temperature of the treated tissue because the nanothermometers used for thermal feedback, based on a spectral analysis of emitted radiation, were affected by the inhomogeneous extinction of the tissues. This work shows how this deficiency can be overcome by using core-shell-shell nanostructures doped with lanthanide ions (Nd^{3+} and Yb^{3+}). Thermal reading was achieved from the analysis of the Yb^{3+} luminescence lifetime whereas simultaneous heating was achieved thanks to the non-radiative deexcitations of Nd^{3+} ions. Simple proof-of-concept experiments show the great potential of these lanthanide-doped nanostructures for the development of in vivo photo-thermal treatments with absolute and reliable thermal feedback.

1. Introduction

Photothermal therapy (PTT) consists in the use of laser radiation to cause an increase in the temperature of malignant tissues [1,2]. This laser radiation is less energetic than the one used in other light-based therapies (e.g. photodynamic therapy) and is, therefore, less harmful to surrounding cells and tissues [3]. If the laser radiation raises the tissue temperature above 42 °C, a series of processes involving protein denaturalization occurs, which are often irreversible [4]. These processes may induce transitory states in cells, characterized by a lower defense capacity against the action of drugs or radiation, or directly trigger cell apoptosis. In the case of cancer cells, this causes a greater responsiveness to treatments such as chemotherapy or radiotherapy [5,6]. Therefore, PTT can complement traditional treatments. In stark

contrast, if the induced temperature far exceeds 42 °C, the death of irradiated cells can be directly induced. Consequently, laser radiation could stop the development of tumors by selectively destroying the cancer cells.

PTT has undergone a rapid development in recent years, largely due to the use of heating nanoparticles [7]. These are nanoparticles with high light-to-heat conversion efficiencies: they effectively absorb laser radiation and transform a large fraction into heat [8]. The fundamental advantage of using nanoheaters (NHs) is that they make specific and local PTT possible [9]. For this, it is necessary for the NHs to preferentially accumulate in the tissue to be treated (usually tumors), which can be achieved with an adequate functionalization of their surface [10,11]. Once accumulated in the tissue to be treated, the irradiated NHs transform the light that penetrates the tumor into heat, thus triggering PTT.

* Corresponding author. Nanomaterials for Bioimaging Group (NanoBIG), Departamento de Física de Materiales, Facultad de Ciencias, Universidad Autónoma de Madrid, Madrid, 28049, Spain.

E-mail address: daniel.jaque@uam.es (D. Jaque).

The use of NHs in PTT has two main consequences: firstly, the intensity of the laser radiation required to achieve therapeutic levels of temperature is reduced [12], and secondly, only those tissues in which the NHs are located will experience a significant temperature rise [13].

There are a large number of nanosized materials that can act as photothermal agents including non-luminescent NHs (such as gold nanoparticles [14]) and luminescent NHs (LNHs such as quantum dots [15] or nanoparticles doped with lanthanide ions [16]). The use of LNHs has advanced PTT as their luminescence can be used not only to locate the treated tissue [17,18] but also in certain cases, to determine remotely and in real-time the magnitude of the induced heating [19,20]. In turn, the latter makes it possible to adjust the parameters of the therapy (such as the laser intensity or the treatment time) so that the temperatures do not reach harmful levels for the adjacent healthy tissues. In these cases, thermal control is achieved thanks to luminescent thermometry, which works by obtaining a temperature reading based on the analysis of the generated luminescence [21]. For this, it is necessary for the employed particles to show not only a high heat-generation efficiency but also highly temperature-dependent luminescence properties. In most cases, the temperature readout is obtained from the analysis of the emission spectra based on the temperature dependence of the emitted intensity or, alternatively, on the temperature-induced changes in the shape of the emission spectra (ratiometric approach) [22,23]. Based on these strategies, LNHs have already been used for controlled PTT of tumors in small-animal models [24].

Despite the great advances made possible by the LNHs used till now, they present a major drawback: their thermal feedback is based on the analysis of emission spectra which are subject to tissue-induced spectral distortions, making the thermal readout unreliable. Even in the best-case scenario, where tissue-induced spectral distortions are previously characterized and the original spectral shape may be reconstructed, spectrum-based LNHs are only capable of providing information about the temperature increase caused by laser radiation. They, thus, fail to provide an absolute and reliable temperature readout [25].

Recent works have shown how these limitations can be overcome by using the luminescence lifetime as temperature indicator as it is not affected by tissue extinction. In particular, it has been demonstrated that

Nd^{3+} and Yb^{3+} doped dielectric nanoparticles show a luminescence lifetime strongly dependent on the temperature, which has allowed accurate, reliable and absolute temperature reading at small animal level [26]. Nevertheless, their ability for heat generation under laser excitation while providing a thermal feedback based on their luminescence lifetime (schematically represented in Fig. 1) is still not demonstrated.

In this work, we have synthesized Nd^{3+} and Yb^{3+} co-doped multi-layered $\beta\text{-NaYF}_4@\beta\text{-NaYF}_4$: 60% Nd^{3+} , 20% Yb^{3+} @ CaF_2 nanoparticles that efficiently convert infrared laser radiation into heat thanks to their high Nd^{3+} content. Such structures also show a strong temperature-dependent lifetime so the absolute magnitude of the laser-induced heating can be measured. Straightforward experiments demonstrate the potential of these structures for safe and efficient PTT. Limitations and future improvement directions are also discussed.

2. Results and discussion

The Nd^{3+} and Yb^{3+} doped nanoparticles used in this work were synthesized following the work of M. Tan and co-workers [26]. The nanoparticles are constituted by an inert $\beta\text{-NaYF}_4$ core covered by an active $\beta\text{-NaYF}_4$ shell doped with Yb^{3+} and Nd^{3+} ions. This inactive-core/active-shell structure was ultimately shielded by an inert shell of CaF_2 . These nanostructures have recently demonstrated an excellent performance as lifetime-based luminescent nanothermometers capable, for example, of monitoring the thermal impact of inflammatory processes at the small animal level. In this work, we set the Nd^{3+} and Yb^{3+} concentrations to 60 and 20 mol % respectively. These concentrations allow to reach high light-to-heat conversion efficiency, as the high Nd^{3+} content ensures dominant non-radiative transitions based on high cross-relaxation probabilities and efficient energy-migration from Nd^{3+} ions to quenching centers. The use of CaF_2 as the outer layer is motivated by the intrinsic properties of CaF_2 such as cost-effective, large transparency in a wide spectral range, good lattice match with the core material ($\beta\text{-NaYF}_4$) and, finally, good chemical stability [27].

Fig. 2A includes a series of transmission electron microscopy (TEM) images corresponding to the three stages of the synthesis procedure. As can be observed the inner $\beta\text{-NaYF}_4$ core has a spherical geometry with an

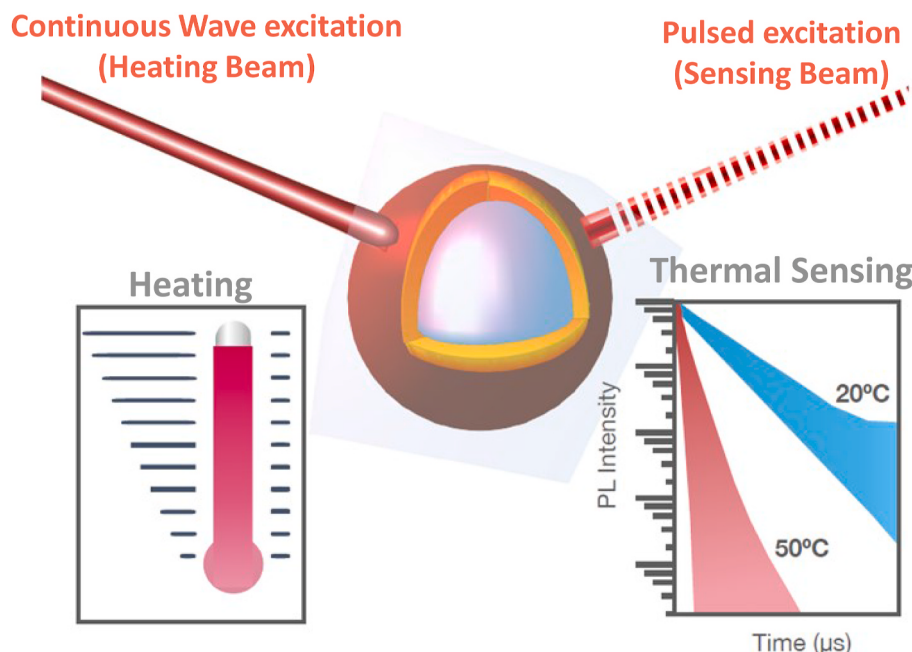


Fig. 1. Schematic representation of a nanoparticle capable of simultaneous local heating and temperature reading when using an excitation beam composed of a continuous and a pulsed laser component, the first one being responsible for the heating and the second one for the temperature readings by means of the lifetime analysis.

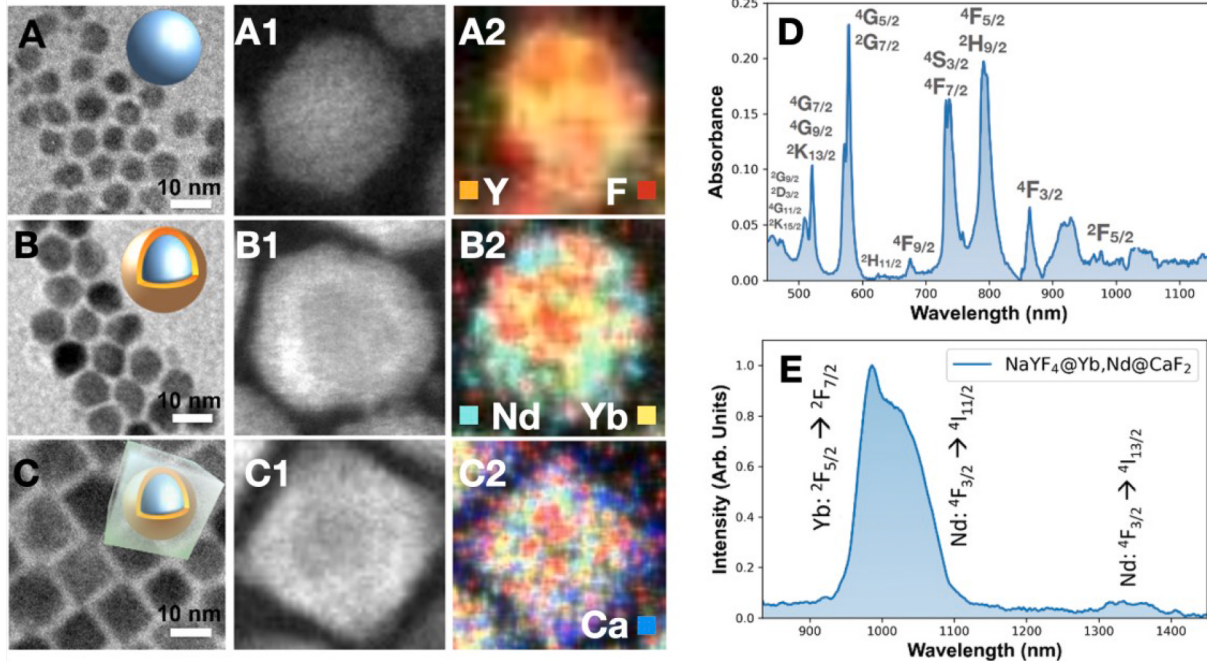


Fig. 2. Transmission electron microscopy (TEM) images of the core (A), core-shell (B) and core-shell-shell (C) nanoparticles used in this work. The inset A1, B1 and C1 depict a detailed HAADF-STEM image of each nanostructure whereas the insets A2, B2 and C2 represent the elemental mapping analysis of the nanoparticles. D) Absorption spectrum of the Nd³⁺ and Yb³⁺ co-doped core-shell-shell nanoparticles. The Nd³⁺ and Yb³⁺ content were set to 60% and 20%, respectively. E) Room temperature emission spectra of Nd³⁺ and Yb³⁺ co-doped core-shell-shell nanoparticles obtained under 800 nm optical excitation. The electronic transitions corresponding to the different bands observed are labeled.

average radius of 7 nm. The active shell also adopts a spherical shape, and the analysis of the TEM images reveals an average thickness of this active shell around 10 nm. Finally, the CaF₂ protective shell shows a cubic shape with a side length close to 12 nm. Fig. 2B includes the

absorption spectrum of the β-NaYF₄@β-NaYF₄: 60% Nd³⁺, 20% Yb³⁺@CaF₂ NPs revealing the presence of the characteristic absorption bands corresponding to transitions between the electronic levels of Nd³⁺ and Yb³⁺ ions. Of special importance is the intense absorption band of

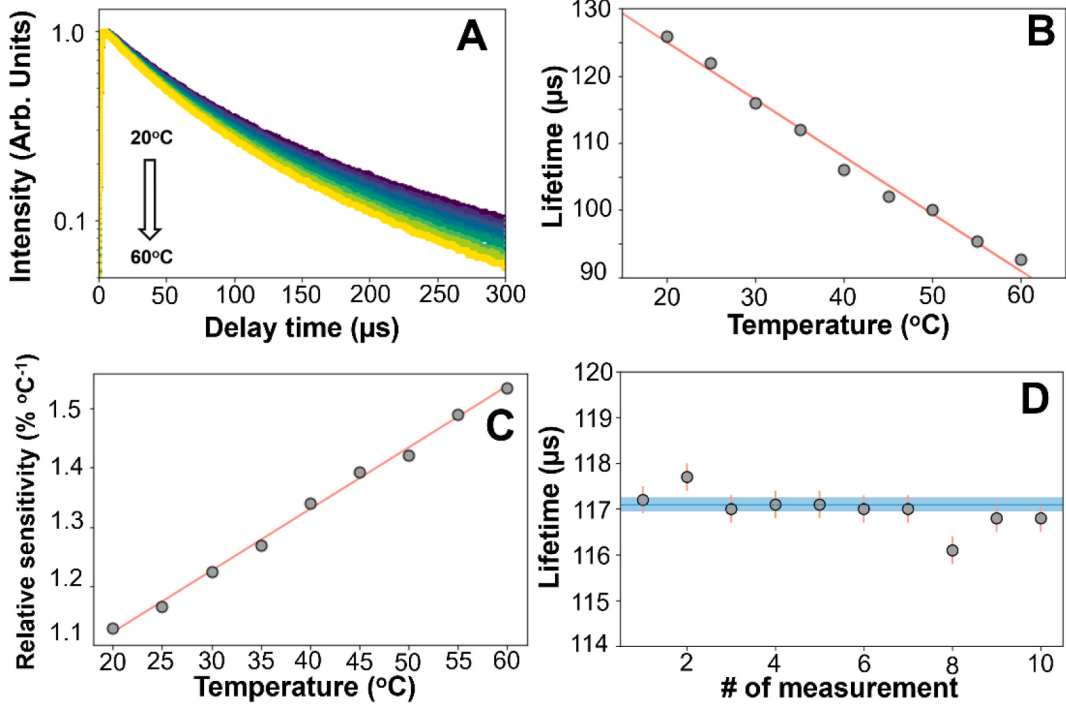


Fig. 3. A) Lifetime decay curves at different temperatures from 20 °C to 60 °C. B) Lifetime values calculated from the previous curves versus temperature. C) Temperature dependence of the relative thermal sensitivity as calculated from data included in B. D) Lifetime values from ten consecutive measurements at a fixed temperature of 20 °C. The blue bar indicates the mean lifetime value (117 μs) and the standard deviation calculated from the consecutive acquisitions ($\pm 0.3 \mu\text{s}$). (For interpretation of the references to colour in this figure legend, the reader is referred to the Web version of this article.)

Nd^{3+} ions at around 800 nm corresponding to the $^4\text{I}_{9/2} \rightarrow ^4\text{F}_{5/2}$ transition of ions. This enables the optical excitation of the nanostructure by using the cost-effective laser diodes operating at around 800 nm as well as operation in the first biological window, located between 700 and 950 nm [28]. This, in turn, makes it possible to maximize the penetration depth into tissues, which is essential for both *in vivo* imaging and therapy. Fig. 2C shows the emission spectrum corresponding to $\beta\text{-NaYF}_4@\beta\text{-NaYF}_4$: 60% Nd^{3+} , 20% Yb^{3+} @ CaF_2 NPs under 808 nm continuous wave (CW) optical excitation. The emission spectrum is mainly constituted by the broadband emission of Yb^{3+} ions expanding from 950 up to 1100 nm. Although 800 nm radiation promotes the excitation of Nd^{3+} ions, their contribution to the emission is marginal (see the weak emission band at around 1350 nm). This emission spectrum can be explained considering two different phenomena: i) The existence of an efficient $\text{Nd}^{3+} \rightarrow \text{Yb}^{3+}$ energy transfer in $\beta\text{-NaYF}_4@\beta\text{-NaYF}_4$: 60% Nd^{3+} , 20% Yb^{3+} @ CaF_2 nanocrystals [29], and ii) The high Nd^{3+} content used in this work causes a relevant quenching of neodymium luminescence due to a high cross-relaxation and energy migration between neodymium ions at a close distance that favors final energy transfer to a quenching center (defect). Both cross-relaxation and energy migration to a quenching center favor the light to heat conversion [16].

Fig. 3A shows the time-dependence of the infrared luminescence generated by a colloidal dispersion of $\beta\text{-NaYF}_4@\beta\text{-NaYF}_4$: 60% Nd^{3+} , 20% Yb^{3+} @ CaF_2 obtained at different temperatures. The intensity curves were obtained after excitation with 10 ns pulses at a wavelength of 800 nm and by collecting the emitted intensity at 980 nm. In all the cases, the 980 nm emitted intensity shows a fast initial rise that is followed by a slower decay. According to previous works the initial intensity rise corresponds to the population of the Yb^{3+} excited state due to energy transfer from the donor ions (Nd^{3+} ions) whereas the long decay is originated by the gradual de-excitation of acceptor (Yb^{3+}) ions. The rise time, corresponding to the luminescence lifetime of Nd^{3+} ions has been found to be roughly independent of temperature, presenting a mean value of $\tau_{\text{rise}} = 0.25 \pm 0.02 \mu\text{s}$. On the other hand, the experimental data reveals that the Yb^{3+} decay time suffers from a strong shortening when increasing temperature. This behavior has also been observed in previous works [26]. Although it has not been explained in detail, we state that the observed reduction in the Yb^{3+} luminescence lifetime is very likely correlated with the thermal activation of the $\text{Yb}^{3+} \rightarrow \text{Nd}^{3+}$ back energy transfer that emerges as an additional de-excitation path for Yb^{3+} ions. The decay curve of ytterbium ions deviates from a single exponential decay. This is probably caused by the existence of cross-relaxation and energy migration between ytterbium ions together with surface-related non-radiative decays. In this case (non-exponential decays) the best criterion to determine the luminescence lifetime is to use the average lifetime as calculated by integrating the decay curve. In this case, the average luminescence lifetime ($\langle \tau_{\text{yb}} \rangle$) is defined as:

$$\langle \tau_{\text{yb}} \rangle = \frac{\int I(t) \cdot t \cdot dt}{\int I(t) \cdot dt} \quad (1)$$

where $I(t)$ is the luminescence intensity at time t after pulsed excitation. This definition is usually applied to pure decay curves (i.e., in absence of any initial intensity rise). In our case, as mentioned above, the decay curves do show an initial rise due to the population of the metastable state of neodymium (donor) ions. Despite this fact, we have adopted this definition for the sake of simplicity in the analysis of experimental data. This approximation is supported by the fact that the rise time ($<1 \mu\text{s}$) is much shorter than the decay time of ytterbium ions (close to $100 \mu\text{s}$) so that the integrals in expression (1) are dominated by the ytterbium decay [30]. Fig. 3b shows the temperature dependence of the Yb^{3+} lifetime as obtained by fitting the experimental data included in Fig. 3A-D only for times longer than the rise time to a single exponential decay. As can be observed, the Yb^{3+} luminescence decay time reduces

with temperature. We can now calculate the relative thermal sensitivity as $S_r = \frac{1}{\tau_{\text{yb}}(T)} \frac{d\tau_{\text{yb}}(T)}{dT}$, where $\tau_{\text{yb}}(T)$ is the luminescence decay time of Yb^{3+} ions at temperature T . Fig. 3C includes the temperature dependence of the relative thermal sensitivity of $\beta\text{-NaYF}_4@\beta\text{-NaYF}_4$: 60% Nd^{3+} , 20% Yb^{3+} @ CaF_2 . The relative thermal sensitivity increases pseudo-linearly with temperature in the investigated range of temperatures (20–60 °C). At 37 °C, the relative thermal sensitivity has been found to be close to $1.3\% \text{ }^{\circ}\text{C}^{-1}$, a value that is comparable to the thermal sensitivities previously reported for other lifetime-based luminescent nanothermometers such as Ag_2S nanoparticles ($3\% \text{ }^{\circ}\text{C}^{-1}$) [31], CdTe quantum dots ($1.7\% \text{ }^{\circ}\text{C}^{-1}$) [32] or upconverting nanoparticles ($1.5\% \text{ }^{\circ}\text{C}^{-1}$) [33,34]. Although our $\beta\text{-NaYF}_4@\beta\text{-NaYF}_4$: 60% Nd^{3+} , 20% Yb^{3+} @ CaF_2 NPs showed similar relative thermal sensitivities than other lifetime-based thermal sensors they show clear advantages such as their operation in the second biological window (essential for *in vivo* applications) and their lifetimes in the $100 \mu\text{s}$ range (that make lifetime thermal imaging possible employing conventional laser diodes, infrared cameras, and time-gating protocols). Fig. 3D shows the luminescence decay time of Yb^{3+} ions obtained from consecutive measurements at a fixed temperature (20 °C). From these data, we have estimated our uncertainty in the determination of the luminescence lifetime. The standard deviation calculated from these consecutive measurements has been estimated to be close to $0.3 \mu\text{s}$ (i.e., close to a relative error of 0.25%). This systematic/experimental error in the determination of the luminescence decay time yields to a temperature uncertainty close to 0.4 °C. This is, indeed, more than enough for monitoring hyperthermia treatments in which the temperature changes are expected to be of several degrees, i.e. well above our thermal resolution. Note that data displayed in Fig. 3D were obtained by continuously illuminating the colloidal dispersion of $\beta\text{-NaYF}_4@\beta\text{-NaYF}_4$: 60% Nd^{3+} , 20% Yb^{3+} @ CaF_2 NPs. Experimental data did not reveal any trend indicating that the irradiation with the pulsed probe beam does not cause any significant heating. This was, indeed, expected since the probe pulsed beam (1.5 mJ pulse energy and 10 Hz repetition rate) has a low average laser power (<15 mW).

Once the sensing capabilities of $\beta\text{-NaYF}_4@\beta\text{-NaYF}_4$: 60% Nd^{3+} , 20% Yb^{3+} @ CaF_2 NPs have been demonstrated, we evaluated their heating capacities. Fig. 4a includes a series of infrared thermal images of a solution of $\beta\text{-NaYF}_4@\beta\text{-NaYF}_4$: 60% Nd^{3+} , 20% Yb^{3+} @ CaF_2 under optical excitation with an 808 nm continuous-wave laser providing different laser intensities. For comparison, the thermal images obtained under the same experimental conditions (i.e., solution volume and laser irradiation intensities) when the $\beta\text{-NaYF}_4@\beta\text{-NaYF}_4$: 60% Nd^{3+} , 20% Yb^{3+} @ CaF_2 solution is replaced by water are included. It is evidenced how the presence of these nanoparticles leads to a clear temperature increase in the solution. This reveals the light-to-heat conversion capability of $\beta\text{-NaYF}_4@\beta\text{-NaYF}_4$: 60% Nd^{3+} , 20% Yb^{3+} @ CaF_2 . Although the study of the mechanisms leading to this light-to-heat conversion is out of the scope of this work we postulate that it is related to the non-radiative de-excitation of Nd^{3+} ions that is favored by their high concentration. This makes cross-relaxation and energy migration to quenching defects possible, enlarging the fraction of absorbed power that is finally converted into heat. Fig. 4B includes the temperature of the $\beta\text{-NaYF}_4@\beta\text{-NaYF}_4$: 60% Nd^{3+} , 20% Yb^{3+} @ CaF_2 solution obtained with infrared thermal camera for the different laser power densities. The temperature of the dispersion is found to increase linearly with laser power density, as expected. It can be noted that this temperature corresponds to the temperature increase caused in the tube containing the $\beta\text{-NaYF}_4@\beta\text{-NaYF}_4$: 60% Nd^{3+} , 20% Yb^{3+} @ CaF_2 dispersion as the thermal camera is only capable of surface temperature sensing. Thermal cameras, in fact, fail to provide a reading of the internal solution temperature. In any case, data included in Fig. 4 evidence the heating capacity of our $\beta\text{-NaYF}_4@\beta\text{-NaYF}_4$: 60% Nd^{3+} , 20% Yb^{3+} @ CaF_2 .

Fig. 5A shows a schematic representation of the experimental setup used in this work to demonstrate the potential use of our $\beta\text{-NaYF}_4@\beta\text{-NaYF}_4$:

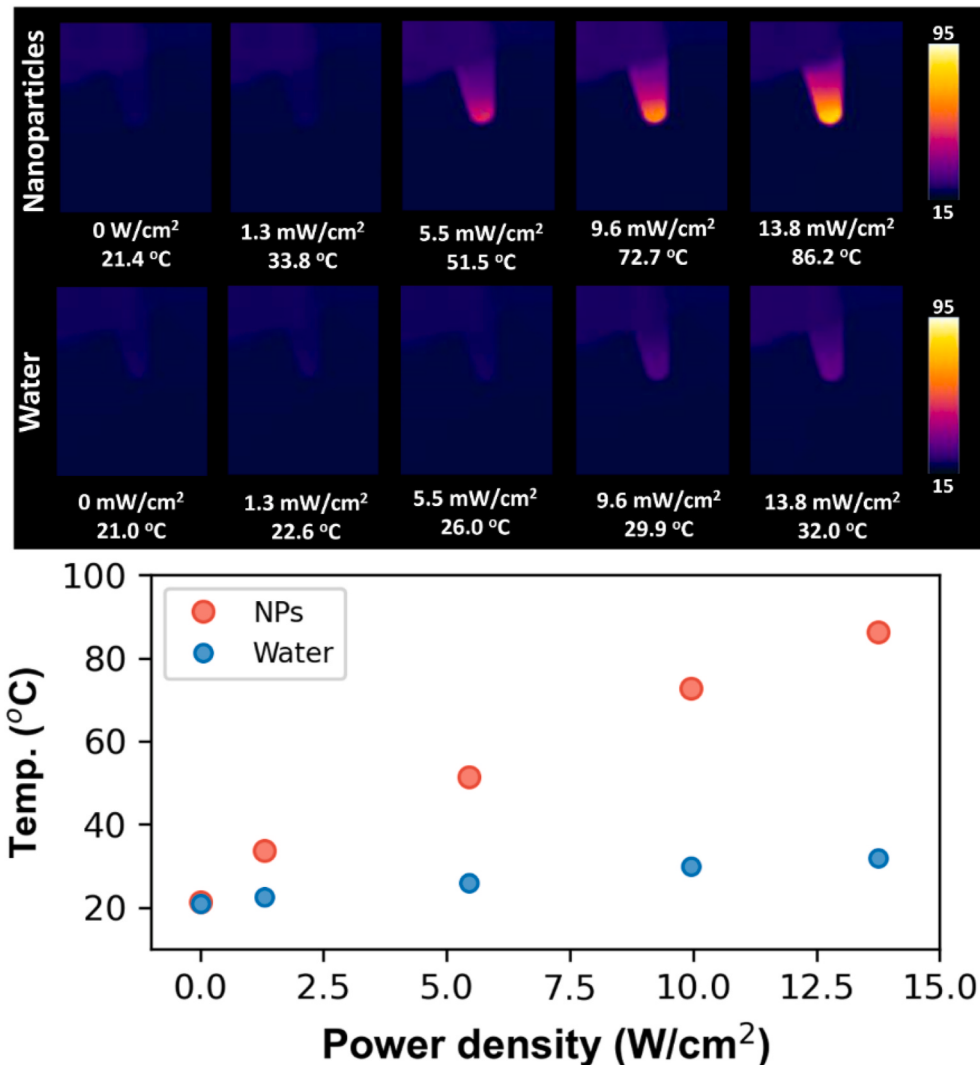


Fig. 4. Thermal images of two microtubes filled with a 20 μL aqueous suspension of $\beta\text{-NaYF}_4@ \beta\text{-NaYF}_4$: 60% Nd^{3+} , 20% Yb^{3+} @ CaF_2 NPs at a concentration of 2 mg/mL or 20 μL of water, respectively. In both cases, the microtube was illuminated with a continuous wave 808 nm laser of different power densities. Error bars were substituted with bigger data points in order to cover more than the small and less accurate digital error of the thermal camera used in this experiment.

NaYF_4 : 60% Nd^{3+} , 20% Yb^{3+} @ CaF_2 NPs for simultaneous heating and lifetime-based thermal sensing. The aqueous solution of $\beta\text{-NaYF}_4@ \beta\text{-NaYF}_4$: 60% Nd^{3+} , 20% Yb^{3+} @ CaF_2 NPs were placed inside a microtube. Heating was induced by irradiating the dispersion with a fiber-coupled 808 nm diode. Simultaneously, a second laser (800 nm wavelength and 10 ns pulse width) was used for transient excitation of the $\beta\text{-NaYF}_4@ \beta\text{-NaYF}_4$: 60% Nd^{3+} , 20% Yb^{3+} @ CaF_2 NPs. The luminescence generated by the nanoparticles in the microtube was collected by a set of lenses, spectrally filtered by a compact monochromator and finally detected by an infrared photomultiplier tube connected to a digital oscilloscope. The compact monochromator was set to 980 nm so only the luminescence emitted by Yb^{3+} ions was registered. In our experimental conditions, the acquisition of a high signal-to-noise ratio decay curve requires an average of 500 curves. With the 10 Hz repetition rate of the excitation laser, each measurement requires 50 s. Substantial reduction of these long acquisition times is one of the main challenges to be faced in the near future. Fig. 5B shows the Yb^{3+} luminescence decay curves obtained in absence of CW 800 nm laser excitation and under CW 800 nm laser excitation with a laser power density of 14 W/cm^2 . Note that in presence of the CW laser irradiation, the luminescence decay becomes faster, indicating a relevant heating of the $\beta\text{-NaYF}_4@ \beta\text{-NaYF}_4$: 60% Nd^{3+} , 20% Yb^{3+} @ CaF_2 NPs. The reduction in the Yb^{3+} luminescence

lifetime has been found to follow a monotonous trend with the 800 nm laser irradiation density as can be observed in Fig. 5C. The actual local temperature of $\beta\text{-NaYF}_4@ \beta\text{-NaYF}_4$: 60% Nd^{3+} , 20% Yb^{3+} @ CaF_2 NPs can be, indeed, known by converting the luminescence lifetime into temperature by using the calibration dataset of Fig. 3B. Results are included in Fig. 5D revealing a linear increment of the temperature of $\beta\text{-NaYF}_4@ \beta\text{-NaYF}_4$: 60% Nd^{3+} , 20% Yb^{3+} @ CaF_2 NPs with the 800 nm CW laser power density, as it was expected. Note that for the maximum laser power density used in this work (14 W/cm^2) the analysis of the decay curves revealed a nanoparticle temperature close to 80 °C. This is, indeed, in excellent agreement with the data obtained by using the infrared thermal camera also revealing a microtube temperature close to 80 °C for an 800 nm continuous wave laser power of 14 W/cm^2 . Results included in Fig. 5D were obtained by extrapolating the calibration data of Fig. 3B up to temperatures of 80 °C. This good agreement reveals that the extrapolation of the calibration data of Fig. 3B up to temperatures of 80 °C is reasonable. In addition, the good agreement with the data obtained with the thermal camera reveals that $\beta\text{-NaYF}_4@ \beta\text{-NaYF}_4$: 60% Nd^{3+} , 20% Yb^{3+} @ CaF_2 NPs are reliable absolute temperature sensors and that in our experimental conditions the temperature of individual nanoparticles (local temperature) is basically the same than the solution temperature (that measured by the thermal camera). A detailed analysis

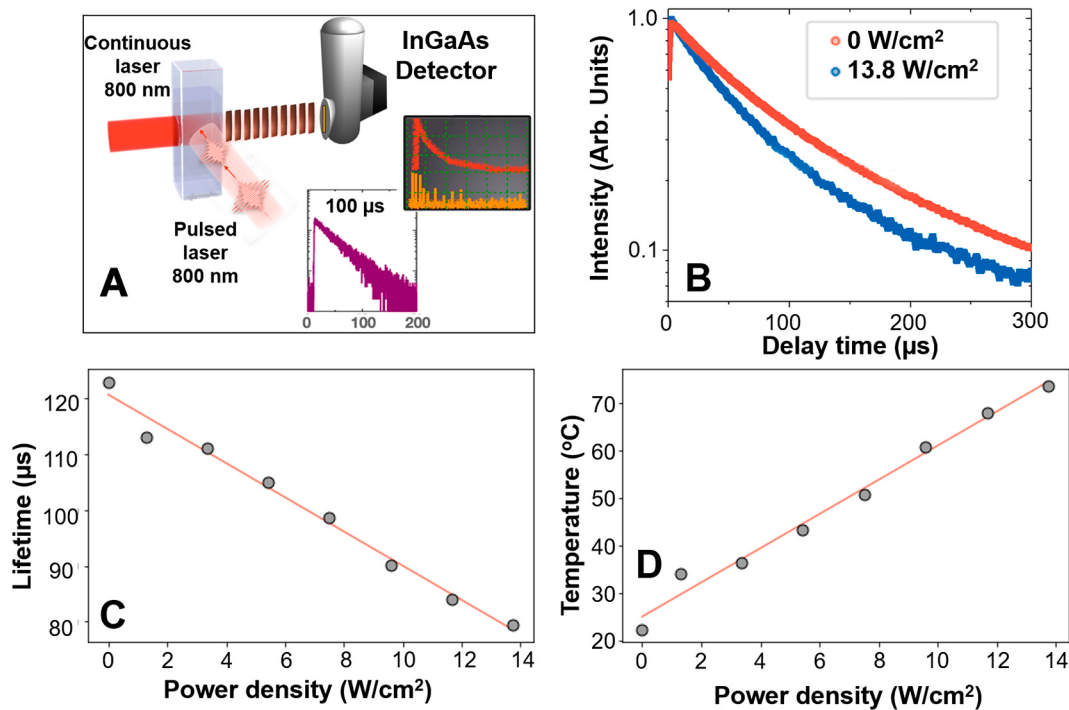


Fig. 5. **A)** Schematic representation of the experiments designed to demonstrate the capability of $\beta\text{-NaYF}_4@\beta\text{-NaYF}_4$: 60% Nd³⁺, 20% Yb³⁺@CaF₂ for simultaneous heating and reliable and absolute thermal feedback. Note that $\beta\text{-NaYF}_4@\beta\text{-NaYF}_4$: 60% Nd³⁺, 20% Yb³⁺@CaF₂ NPs are excited with a CW + pulsed laser beam and the thermal feedback is obtained by analyzing the AC component of luminescence. **B)** Intensity decay curves obtained in absence of CW excitation and when the CW excitation power density was set to 14 W/cm². Note the visible shortening of the luminescence lifetime indicating relevant local heating. **C)** Luminescence lifetime of $\beta\text{-NaYF}_4@\beta\text{-NaYF}_4$: 60% Nd³⁺, 20% Yb³⁺@CaF₂ NPs as obtained for different CW laser power densities. **D)** Temperature of $\beta\text{-NaYF}_4@\beta\text{-NaYF}_4$: 60% Nd³⁺, 20% Yb³⁺@CaF₂ NPs for different CW laser power densities calculated from the data included in C) and by using the calibration curve of Fig. 2B.

of the data included in Fig. 5D also reveals that increasing local temperature by 5 °C (as that required for hyperthermia treatments) requires a laser power density slightly larger than 1 W/cm². Although this laser power density is adequate for in vivo experiments, it would be desirable to reduce it by increasing the light-to-heat conversion efficiency of $\beta\text{-NaYF}_4@\beta\text{-NaYF}_4$: 60% Nd³⁺, 20% Yb³⁺@CaF₂ NPs. There are several ways to increase the heating efficiency of our nanoparticles including the increase of the Nd³⁺ content to simultaneously increase the absorption efficiency and the non-radiative decay probabilities. In addition, the use of an Nd³⁺ doped core instead of an inert one would also increase the heating efficiency of the nanoparticles. All these possibilities will be explored in future works.

3. Conclusions

In summary, we have demonstrated how it is possible to design lanthanide-doped core-shell-shell nanoparticles capable of simultaneous heating and thermal sensing under infrared laser excitation. In particular, we have provided experimental evidence of how $\beta\text{-NaYF}_4@\beta\text{-NaYF}_4$: 60% Nd³⁺, 20% Yb³⁺@CaF₂ NPs are capable of converting continuous wave 800 nm laser radiation into heat thanks to the existence of non-radiative de-excitations of both Nd³⁺ and Yb³⁺ ions. In addition, we also demonstrated the strong temperature dependence of the luminescence decay time of Yb³⁺ ions that, can be used for absolute and remote thermal sensing. Straightforward experiments have been designed to demonstrate that both effects (heating and thermal sensing) can be produced simultaneously. We have demonstrated how a simple analysis of decay curves can provide an accurate and absolute readout of local (nanoparticle) temperature.

The results included in this work open a new path towards the development of in vivo photothermal treatments with real-time, fine and absolute thermal control over treated tissues. Prior to their application

in small animal models, the $\beta\text{-NaYF}_4@\beta\text{-NaYF}_4$: 60% Nd³⁺, 20% Yb³⁺@CaF₂ NPs requires further optimization towards the improvement in their heating efficiency and lifetime-based thermal sensitivity. Such optimization will involve optimizing the lanthanide concentration as well as the possibility of changing the lanthanide ion doping of the core.

Credit author statement

Gabriel López-Peña: Investigation, Visualization, Data curation, Writing – review & editing. **Khouloud Hamraoui:** Investigation, Resources. **Karima Horchani-Naifer:** Investigation, Resources. **Christoph Gerke:** Investigation, Writing – review & editing, Resources. **Dirk H. Ortgies:** Investigation, Data curation, Supervision. **Emma Martín Rodríguez:** Investigation, Visualization, Data curation, Supervision. **Guanying Chen:** Writing – review & editing, Resources. **Daniel Jaque:** Writing- Original draft preparation, Project administration. **Jorge Rubio Retama:** Writing- Original draft preparation, Visualization, Writing – review & editing, Resources

Declaration of competing interest

The authors declare that they have no known competing financial interests or personal relationships that could have appeared to influence the work reported in this paper.

Acknowledges

This work was supported by the Ministerio de Ciencia, Innovación y Universidades de España under projects PID2019-106211RB-I00 and MAT2017-83111R by the Comunidad Autónoma de Madrid (S2017/BMD-3867 RENIM-CM) and co-financed by the European Structural and investment fund. Additional funding was provided by the European

Union's Horizon 2020 FET Open programme (Grant Agreement No. 801305, NanoTBTech), and also by COST action CA17140. CG acknowledges the support of the European Commission through the European Union's Horizon 2020 research and innovation program under the Marie Skłodowska-Curie Grant agreement N° 895932 (SPOT).

References

- [1] W. Yang, H. Liang, S. Ma, D. Wang, J. Huang, Gold nanoparticle based photothermal therapy: development and application for effective cancer treatment, *Sustain. Mater. Technol.* 22 (2019), e00109, <https://doi.org/10.1016/j.susmat.2019.e00109>.
- [2] M.I. Khot, H. Andrew, H.S. Svavarsdottir, G. Armstrong, A.J. Quyn, D.G. Jayne, A review on the scope of photothermal therapy-based nanomedicines in preclinical models of colorectal cancer, *Clin. Colorectal Cancer* 18 (2019) e200–e209, <https://doi.org/10.1016/j.clcc.2019.02.001>.
- [3] R. Bhole, C. Bonde, P. Kadam, R. Wavwale, A comprehensive review on photodynamic therapy (PDT) and photothermal therapy (PTT) for cancer treatment, *Turk Onkol. Derg.* 36 (2021) 125–132, <https://doi.org/10.5505/tjo.2020.2400>.
- [4] H. Norouzi, K. Khoshgard, F. Akbarzadeh, In vitro outlook of gold nanoparticles in photo-thermal therapy: a literature review, *Laser Med. Sci.* 33 (2018) 917–926, <https://doi.org/10.1007/s10103-018-2467-z>.
- [5] B.L. Fay, J.R. Melamed, E.S. Day, Nanoshell-mediated photothermal therapy can enhance chemotherapy in inflammatory breast cancer cells, *Int. J. Nanomed.* 10 (2015) 6931–6941, <https://doi.org/10.2147/IJN.S93031>.
- [6] Y. Zhang, J. Liu, Y. Yu, S. Chen, F. Huang, C. Yang, J. Chang, L. Yang, S. Fan, J. Liu, Enhanced radiotherapy using photothermal therapy based on dual-sensitizer of gold nanoparticles with acid-induced aggregation, *Nanomed. Nanotechnol. Biol. Med.* 29 (2020), 102241, <https://doi.org/10.1016/j.nano.2020.102241>.
- [7] W. Sheng, S. He, W.J. Seare, A. Almutairi, Review of the progress toward achieving heat confinement—the holy grail of photothermal therapy, *J. Biomed. Opt.* 22 (2017), 080901, <https://doi.org/10.1117/1.jbo.22.8.080901>.
- [8] J.R. Melamed, R.S. Edelstein, E.S. Day, Elucidating the fundamental mechanisms of cell death triggered by photothermal therapy, *ACS Nano* 9 (2015) 6–11, <https://doi.org/10.1021/acsnano.5b00021>.
- [9] V.P. Pattani, J.W. Tunnell, Nanoparticle-mediated photothermal therapy: a comparative study of heating for different particle types, *Laser Surg. Med.* 44 (2012) 675–684, <https://doi.org/10.1002/lsm.22072>.
- [10] X. Wang, C. Yang, Y. Zhang, X. Zhen, W. Wu, X. Jiang, Delivery of platinum(IV) drug to subcutaneous tumor and lung metastasis using bradykinin-potentiating peptide-decorated chitosan nanoparticles, *Biomaterials* 35 (2014) 6439–6453, <https://doi.org/10.1016/j.biomaterials.2014.04.016>.
- [11] B. Albertini, V. Mathieu, N. Iraci, M. Van Woensel, A. Schoubben, A. Donnadio, S. M.L. Greco, M. Ricci, A. Temperini, P. Blasi, N. Wauthoz, Tumor targeting by peptide-decorated gold nanoparticles, *Mol. Pharm.* 16 (2019) 2430–2444, <https://doi.org/10.1021/acs.molpharmaceut.9b00047>.
- [12] K. Yang, J. Wan, S. Zhang, B. Tian, Y. Zhang, Z. Liu, The influence of surface chemistry and size of nanoscale graphene oxide on photothermal therapy of cancer using ultra-low laser power, *Biomaterials* 33 (2012) 2206–2214, <https://doi.org/10.1016/j.biomaterials.2011.11.064>.
- [13] Y. Shen, J. Lifante, E. Ximenes, H.D.A. Santos, D. Ruiz, B.H. Juárez, I. Zubala Gutiérrez, V. Torres Vera, J. Rubio Retama, E. Martín Rodríguez, D.H. Ortgies, D. Jaque, A. Benayas, B. Del Rosal, Perspectives for Ag2S NIR-II nanoparticles in biomedicine: from imaging to multifunctionality, *Nanoscale* 11 (2019) 19251–19264, <https://doi.org/10.1039/c9nr05733a>.
- [14] X. Huang, P.K. Jain, I.H. El-Sayed, Plasmonic photothermal therapy (PPTT) using gold nanoparticles, *Laser Med. Sci.* 23 (2008) 217–228, <https://doi.org/10.1007/s10103-007-0470-x>.
- [15] H. Liu, C. Li, Y. Qian, L. Hu, J. Fang, W. Tong, R. Nie, Q. Chen, H. Wang, Magnetic-induced graphene quantum dots for imaging-guided photothermal therapy in the second near-infrared window, *Biomaterials* 232 (2020), 119700, <https://doi.org/10.1016/j.biomaterials.2019.119700>.
- [16] X. Wang, H. Li, F. Li, X. Han, G. Chen, Prussian blue-coated lanthanide-doped core/shell/shell nanocrystals for NIR-II image-guided photothermal therapy, *Nanoscale* 11 (2019) 22079–22088, <https://doi.org/10.1039/c9nr07973d>.
- [17] Q. Ma, J. Wang, Z. Li, X. Lv, L. Liang, Q. Yuan, Recent progress in time-resolved biosensing and bioimaging based on lanthanide-doped nanoparticles, *Small* 15 (2019) 1–22, <https://doi.org/10.1002/smll.201804969>.
- [18] E. Hemmer, P. Acosta-Mora, J. Méndez-Ramos, S. Fischer, Optical nanoprobes for biomedical applications: shining a light on upconverting and near-infrared emitting nanoparticles for imaging, thermal sensing, and photodynamic therapy, *J. Mater. Chem. B* 5 (2017) 4365–4392, <https://doi.org/10.1039/c7tb00403f>.
- [19] E.C. Ximenes, A.F. Pereira, U. Rocha, W.F. Silva, D. Jaque, C. Jacinto, Thulium doped LaF₃ for nanothermometry operating over 1000 nm, *Nanoscale* 11 (2019) 8864–8869, <https://doi.org/10.1039/c9nr00082h>.
- [20] A. Skripka, A. Benayas, R. Marin, P. Canton, E. Hemmer, F. Vetrone, Double rare-earth nanothermometer in aqueous media: opening the third optical transparency window to temperature sensing, *Nanoscale* 9 (2017) 3079–3085, <https://doi.org/10.1039/c6nr08472a>.
- [21] D. Wawrzynczyk, A. Bednarkiewicz, M. Nyk, W. Strek, M. Samoc, Neodymium(iii) doped fluoride nanoparticles as non-contact optical temperature sensors, *Nanoscale* 4 (2012) 6959–6961, <https://doi.org/10.1039/c2nr32203j>.
- [22] D. Jaque, F. Vetrone, Luminescence nanothermometry, *Nanoscale* (2012), <https://doi.org/10.1039/c2nr30764b>.
- [23] A. Bednarkiewicz, L. Marciniak, L.D. Carlos, D. Jaque, Standardizing luminescence nanothermometry for biomedical applications, *Nanoscale* 12 (2020) 14405–14421, <https://doi.org/10.1039/cdnr03568h>.
- [24] M. Kamimura, T. Matsumoto, S. Suyari, M. Umezawa, K. Soga, Ratiometric near-infrared fluorescence nanothermometry in the OTN-NIR (NIR II/III) biological window based on rare-earth doped β-NaYF₄ nanoparticles, *J. Mater. Chem. B* 5 (2017) 1917–1925, <https://doi.org/10.1039/c7mb00070g>.
- [25] Y. Shen, J. Lifante, N. Fernández, D. Jaque, E. Ximenes, In vivo spectral distortions of infrared luminescent nanothermometers compromise their reliability, *ACS Nano* 14 (2020) 4122–4133, <https://doi.org/10.1021/acsnano.9b08824>.
- [26] M. Tan, F. Li, N. Cao, H. Li, X. Wang, C. Zhang, D. Jaque, G. Chen, Accurate in vivo nanothermometry through NIR-II lanthanide luminescence lifetime, *Small* 16 (2020) 1–10, <https://doi.org/10.1002/smll.202004118>.
- [27] A.L. Pellegrino, G. Lucchini, A. Speghini, G. Malandrino, Energy conversion systems: molecular architecture engineering of metal precursors and their applications to vapor phase and solution routes, *J. Mater. Res.* 35 (2020) 2950–2966, <https://doi.org/10.1557/jmr.2020.253>.
- [28] E. Hemmer, A. Benayas, F. Légaré, F. Vetrone, Exploiting the biological windows: current perspectives on fluorescent bioprobes emitting above 1000 nm, *Nanoscale Horizons* 1 (2016) 168–184, <https://doi.org/10.1039/c5nh00073d>.
- [29] D. Jaque, O. Ramirez, E. Bausá, G. Solé, E. Cavalli, A. Speghini, M. Bettinelli, Nd³⁺ → Yb³⁺ energy transfer in the YAl₃(BO₃)₄ nonlinear laser crystal, *Phys. Rev. B Condens. Matter. Mater. Phys.* 68 (2003) 1–9, <https://doi.org/10.1103/PhysRevB.68.035118>.
- [30] K. Maciejewska, M. Szalkowski, A. Bednarkiewicz, L. Marciniak, From structural phase transition to highly sensitive lifetime based luminescent thermometer: multifaceted modification of thermometric performance in Y 0.9–x Nd x Yb 0.1 PO 4 nanocrystals, *J. Mater. Chem. C* 9 (2021) 15831–15839, <https://doi.org/10.1039/dltc04107j>.
- [31] H.D.A. Santos, D. Ruiz, G. Lifante, C. Jacinto, B.H. Juarez, D. Jaque, Time resolved spectroscopy of infrared emitting Ag₂S nanocrystals for subcutaneous thermometry, *Nanoscale* 9 (2017) 2505–2513, <https://doi.org/10.1039/c6nr08534b>.
- [32] P. Haro-González, L. Martínez-Maestro, I.R. Martín, J. García-Solé, D. Jaque, High-sensitivity fluorescence lifetime thermal sensing based on CdTe quantum dots, *Small* 8 (2012) 2652–2658, <https://doi.org/10.1002/smll.201102736>.
- [33] O.A. Savchuk, P. Haro-González, J.J. Carvajal, D. Jaque, J. Massons, M. Aguiló, F. Díaz, Er:Yb:NaYF₅O up-converting nanoparticles for sub-tissue fluorescence lifetime thermal sensing, *Nanoscale* 6 (2014) 9727–9733, <https://doi.org/10.1039/c4nr02305f>.
- [34] J. Liang, Fast Wide-Field Upconversion Luminescence Lifetime Thermometry Enabled by Single-Shot Compressed Ultrahigh-Speed Imaging, 2021, pp. 1–9, <https://doi.org/10.1038/s41467-021-26701-1>.